



Isotropic, aberration-corrected light sheet microscopy for rapid high-resolution imaging of cleared tissue

Received: 14 March 2025

Accepted: 25 September 2025

Published online: 13 November 2025

Check for updates

Mostafa Aakhte¹✉, Gesine F. Müller¹, Lennart Roos^{1,2,3,4,5}, Joe Li⁶,
Torben Göpel¹, Kurt R. Weiss⁷, Aleyna M. Diniz^{2,3,5,8}, Jan Wenzel^{1,9,10},
Markus Schwaninger^{1,9,10}, Tobias Moser^{1,2,3,5,8} & Jan Huisken^{1,5,6,10}✉

Light-sheet microscopy is ideal for imaging large and cleared tissues, but achieving a high isotropic resolution for a centimeter-sized sample is limited by slow and often aberrated, axially scanned light sheets. Here, we introduce a compact, high-speed light-sheet fluorescence microscope achieving 850 nm isotropic resolution across cleared samples up to 1 cm³ and refractive indices ranging from 1.33 to 1.56. Using off-the-shelf optics, we combine an air objective and a meniscus lens with an axially swept light sheet to achieve diffraction-limited resolution and aberration correction. The effective field of view is increased by twofold by correcting the field curvature of the light sheet using a concave mirror in the remote focusing unit. Adapting the light sheet's motion with a closed-loop feedback enhances the imaging speed by tenfold, reaching 100 frames per second while maintaining resolution and field of view. We benchmark the system performance across scales, from subcellular structure up to centimeter scale, using various clearing methods.

Light-sheet fluorescence microscopy (LSFM) has become a key instrument in modern biology with its confined excitation and its capability to image live, intact biological samples fast and gently^{1–4}. In LSFM, optical sectioning is achieved by two orthogonal optical arms⁵: one projects a laser light sheet into the sample, illuminating a thin section, and the other records the emitted fluorescence light perpendicularly with a camera. This configuration enables simultaneous collection of emitted light across the entire field of view (FOV), surpassing sequential point-scanning methods in photon efficiency and speed. Localized fluorescence excitation at the chosen plane greatly reduces

photobleaching, which is critical for *in vivo* imaging, but LSFM is also an effective method for imaging large and cleared tissues^{6–10}. It enables scientists to obtain high-resolution images across the entire intact sample, crucial for subsequent reconstruction and quantification.

The light-sheet properties, such as its thickness, effective length (Rayleigh length) and intensity distribution in all directions greatly influence image quality. The thickness of the light sheet primarily determines the axial resolution. In contrast, the lateral resolution is determined by the numerical aperture (NA) of the detection objective lens (DL), magnification and camera pixel size^{5,11}. Consequently,

¹Multiscale Biology, Department of Biology and Psychology, University of Göttingen, Göttingen, Germany. ²Institute for Auditory Neuroscience and InnerEarLab, University Medical Center Göttingen, Göttingen, Germany. ³Else-Kröner-Fresenius Center for Optogenetic Therapies, University Medical Center Göttingen, Göttingen, Germany. ⁴Department of Otorhinolaryngology, University Medical Center Göttingen, Göttingen, Germany. ⁵Cluster of Excellence 'Multiscale Bioimaging: from Molecular Machines to Networks of Excitable Cells' (MBExC), University of Göttingen, Göttingen, Germany.

⁶Morgridge Institute for Research, Madison, WI, USA. ⁷Department of Biochemistry, University of Wisconsin, Madison, WI, USA. ⁸Auditory Neuroscience and Synaptic Nanophysiology Group, Max Planck Institute for Multidisciplinary Sciences, Göttingen, Germany. ⁹Center of Brain, Behavior and Metabolism, Institute of Experimental and Clinical Pharmacology and Toxicology, University of Lübeck, Lübeck, Germany. ¹⁰German Research Centre for Cardiovascular Research (DZHK), Partner site Hamburg/Lübeck/Kiel and Göttingen, Göttingen, Germany. ✉e-mail: mostafa.aakhte@uni-goettingen.de; jan.huisken@uni-goettingen.de

the axial resolution can be enhanced by creating thinner light sheets. However, a thinner light sheet becomes shorter, no longer filling the entire FOV. Quantitative multiscale analysis requires the imaging setup to have an isotropic resolution, where the axial and lateral resolutions are the same across the entire FOV and, consequently, the illumination and detection NA need to be identical. Isotropic resolution across a large FOV can be achieved elegantly by rapidly moving a thin light sheet across the FOV using a remote-focusing optical arm—a technique known as axially swept light-sheet microscopy (ASLM)^{12,13}. To record only the thinnest part of the light sheet across the FOV, the camera is oriented such that the rolling shutter direction aligns with the light sheet's propagation direction (Supplementary Video 1). The light sheet is swept across the FOV once during the exposure time of the scientific complementary metal–oxide–semiconductor (sCMOS) camera, with its waist location synchronized to the position of the camera's rolling shutter.

In ASLM, the light sheet can be swept with electrically tunable lenses (ETLs), piezo actuators or voice coil actuators. The concept was introduced initially using a piezo actuator for imaging small live samples, providing an isotropic resolution of 370 nm over a 50- μm FOV at an imaging rate of 6 Hz (ref. 12). ASLM was also adapted to larger cleared samples, as demonstrated in the MesoSPIM platform, which achieved a FOV of 13.29 mm with an isotropic resolution of 6.5 μm (ref. 14). The subsequent benchtop MesoSPIM variant offered an improved resolution, albeit nonisotropic, at 1.5 μm laterally and 3.3 μm axially, with frame rates of 4.5 Hz and 6.5 Hz using ETLs¹⁵. Another setup achieved isotropic resolution up to 380 nm, covering a FOV of 310 $\mu\text{m} \times$ 310 μm and using mechanical tiling to image large samples¹³. This setup employed a voice coil actuator, which provided higher stroke movement in continuous motion, increasing the frame rate to 10 Hz. However, the setups, so far, have not reached the maximum frame rate of the sCMOS camera. The speed, however, is crucial to keep acquisition times within reasonable limits, especially in large tissues where many tiles need to be acquired at high resolution to reconstruct the entire sample.

To support a wide range of applications, the microscope should be compatible with expansion microscopy^{16,17} and many tissue-clearing protocols such as 3DISCO, iDISCO, EZ Clear, and so on^{18–20} and their broad range of refractive indices (RIs), from RI = 1.33 (water) to RI = 1.56 (ethyl cinnamate; ECi). A straightforward approach to image samples with various RIs uses air objective lenses with long working distances^{21,22}. Oily and toxic solvents are then enclosed in a chamber with glass windows, and the air lenses can be exchanged easily without touching the solvent. However, in such a configuration, the lenses induce substantial spherical, chromatic aberrations and field curvature, preventing reaching the diffraction limit. Spherical aberrations can be mitigated by introducing a meniscus lens instead of the flat glass window between the air objective lens and immersion medium²³. An open-top light-sheet microscope^{24,25} used a customized meniscus lens to achieve a near-diffraction-limited light sheet. However, a low NA light sheet in combination with a high NA detection lens limited resolution to 1.1 μm laterally and 2 μm axially with an effective FOV of 780 $\mu\text{m} \times$ 375 μm because of aberrations at the edge of the detection arm.

Field curvature is also a common aberration, limiting the FOV and affecting both the detection and illumination arms. In the detection arm, field curvature results in blur at the edges of the image. On the illumination side, the waist of the light sheet is bent in the presence of field curvature, which is particularly pronounced for high NA. This effect leads to a desynchronization of the waist movement at the FOV edges in ASLM and reduces the usable FOV to a small area where the waist is straight. The field curvature can be addressed by reducing the FOV or designing an expensive custom objective lens²⁶. One can also select lenses with minimum field curvature by measuring their field curvature^{15,27}. Further, the existing field curvature can be adapted by adjusting the light-sheet geometry and using a curved beam²⁸.

Although all the above-mentioned efforts use at least one air objective lens with minimized aberrations, each approach falls short of achieving isotropic submicron resolution over the largest possible FOV.

To overcome all these issues, we have developed a compact, field curvature-corrected light-sheet microscope tailored for imaging cleared tissues. The microscope offers an isotropic resolution of 850 nm in media with RIs ranging from 1.33 to 1.56 at a speed of 100 frames per second to image samples up to 1 cm³ in size. Our innovative design combines a multi-immersion lens, an air objective lens, a meniscus lens and a concave mirror within an ASLM framework. We have doubled the FOV by using a concave mirror to correct the field curvature of the light sheet while maintaining isotropic resolution. Further, we have greatly improved the imaging speed by a factor of ten, compared to the fastest previous microscopes, by precisely controlling the ASLM unit at high frequencies with an optical closed loop. We benchmarked the system performance by imaging various biological samples, including cleared mouse brain, mouse cochlea and zebrafish.

Results

We aimed to achieve an isotropic resolution $<1 \mu\text{m}$ to image submicron structures in large, cleared samples in various media. Hence, the DL needed to have an NA of ≥ 0.4 . Commercially available options included a multi-immersion lens ($\times 16$, NA 0.4, working distance around 12 mm, ASI), which achieves optimal sampling when paired with a 200 mm tube lens and an sCMOS camera with a typical pixel pitch of 6.5 μm (Supplementary Note 1 and Supplementary Fig. 1). This lens is already corrected for chromatic aberrations with constant working distance for different RIs, compatible with various media without the need to realign the lens when changing the medium, making it the ideal choice for the detection lens in our setup.

Conversely, an air objective lens with matching NA = 0.4 served as an ideal illumination lens. We placed it outside the interchangeable sample chamber and its toxic solvents. The air lens can be moved freely during alignment without requiring any sealing. The flexibility of the air illumination objective lens also enabled us to attach the detection lens in a fixed position, sealed to the chamber with a simple O-ring, and its focal plane in the chamber center aligned to the illumination's optical axis. The illumination lens' large working distance (20 mm in air) is beneficial for imaging large samples of a centimeter or more. The chosen Mitutoyo objective lens ($\times 20$ plan apochromat) has an NA of 0.42, which closely matches the detection lens' NA—a prerequisite for achieving isotropic resolution. In addition, in ASLM, to minimize aberrations, the remote-focusing objective lens should ideally be identical to the illumination lens, which was easily achievable with this affordable, long working distance, air objective lens.

Our microscope consists of four main optical components: the laser launch, the ASLM, the illumination arm and the detection arm (Fig. 1a,b, Supplementary Figs. 2–3 and Supplementary Table 2). Briefly, a laser beam with a Gaussian profile enters through the laser launch and is shaped into a light sheet using a cylindrical lens (CL). This light sheet then travels to the ASLM unit, where it is swept by a voice coil and its attached mirror, positioned opposite the ASLM objective lens. The voice coil acts as a single-axis translator, moving rapidly the mirror along the optical axis. Reflecting the primary light sheet through the ASLM and illumination arm results in a shifted light sheet within the chamber. The DL then collects the fluorescence emitted from the sample, and the image is formed by a tube lens on an sCMOS camera with a rolling shutter (Methods).

When using an air objective lens, one of the primary aberrations anticipated is spherical aberration, which prevents the light sheet from achieving the diffraction limit²³ (Fig. 1c, first row). To mitigate spherical aberrations, we introduced an off-the-shelf meniscus lens between the air objective lens and the chamber instead of using a flat glass window. The meniscus lens has a curvature that matches the NA of the illumination beam to allow all the rays to enter the chamber perpendicular

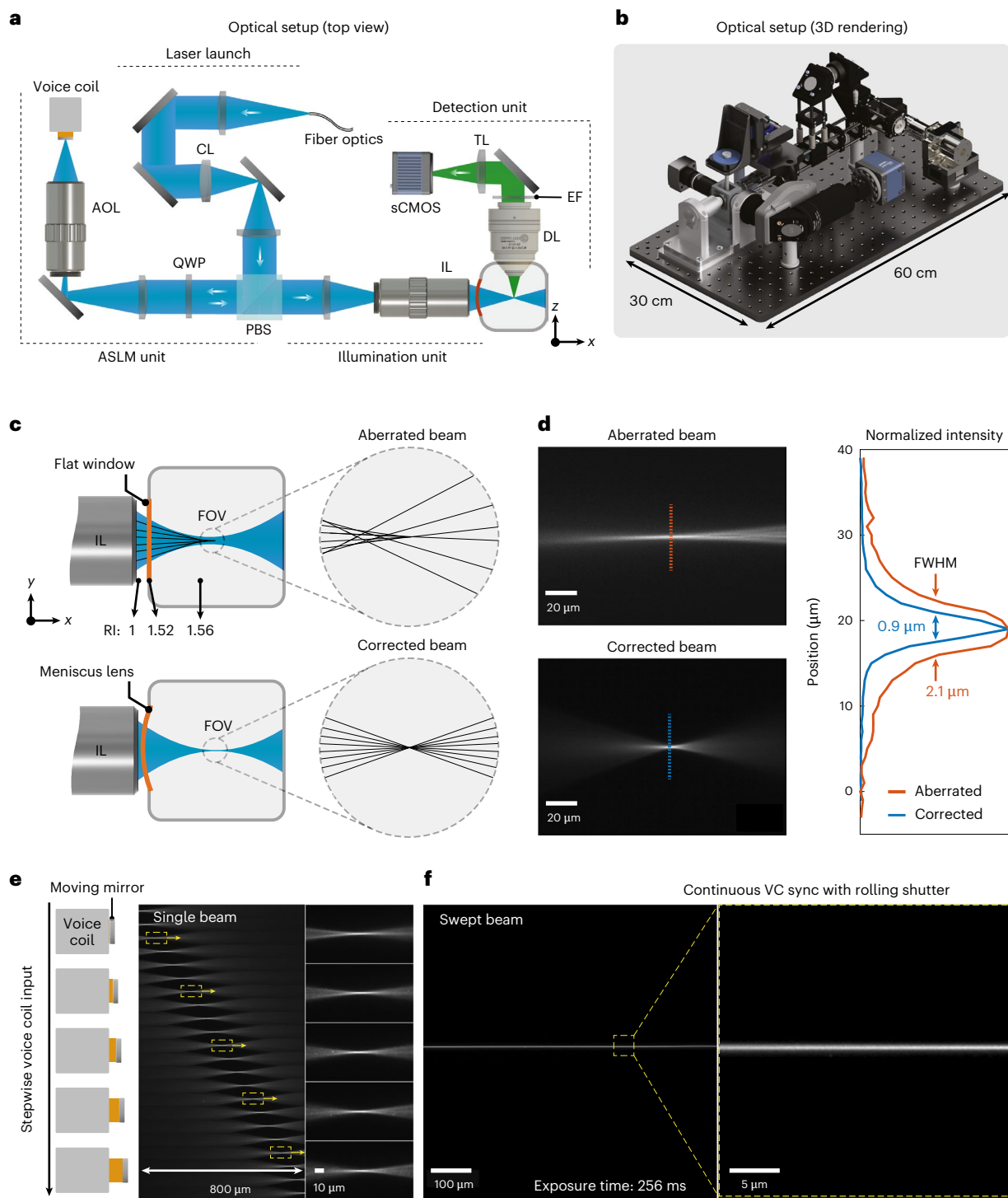


Fig. 1 | Axially swept cleared tissue light-sheet setup and diffraction-limited swept beam. **a**, Optical schematic of the cleared tissue setup from a top view. **b**, 3D rendering of the optical setup in **a**. **c**, Comparison of a glass window and a meniscus lens for correcting spherical aberration in the illumination beam. **d**, Single static beam in a chamber with a flat window and a meniscus lens. The graph shows the beam thickness for both cases. The images are examples from one of ten imaged beams. **e**, Schematic of the voice coil when its input

voltage is changed stepwise. Second and third panels: recorded single beam across the detection FOV, demonstrating the absence of aberrations. **f**, Swept beam with the continuous motion of the voice coil synchronized with the sCMOS rolling shutter. The images are examples from one of five imaged beams. AOL, ASLM objective lens; IL, illumination objective lens; DL, detection objective lens; TL, tube lens; EF, emission filter; FWHM, full-width at half-maximum; PBS, polarizing beam splitter; QWP, quarter-wave plate.

to the glass surface and to minimize refraction (Fig. 1c, second row). Comparing the beam quality, we saw strong spherical aberration when using the flat glass window, whereas it was eliminated greatly with the meniscus lens, reducing the beam size from $2.1 \mu\text{m}$ to 900 nm , the near-diffraction limit (Fig. 1d). We also examined the beam quality

across the detection FOV to ensure it remained aberration-corrected when sweeping the light sheet. We achieved a homogeneous, confined beam across the entire FOV ($800 \mu\text{m} \times 800 \mu\text{m}$) by combining ASLM with the meniscus lens. We then synchronized the swept aberration-corrected beam with the sCMOS rolling shutter during the

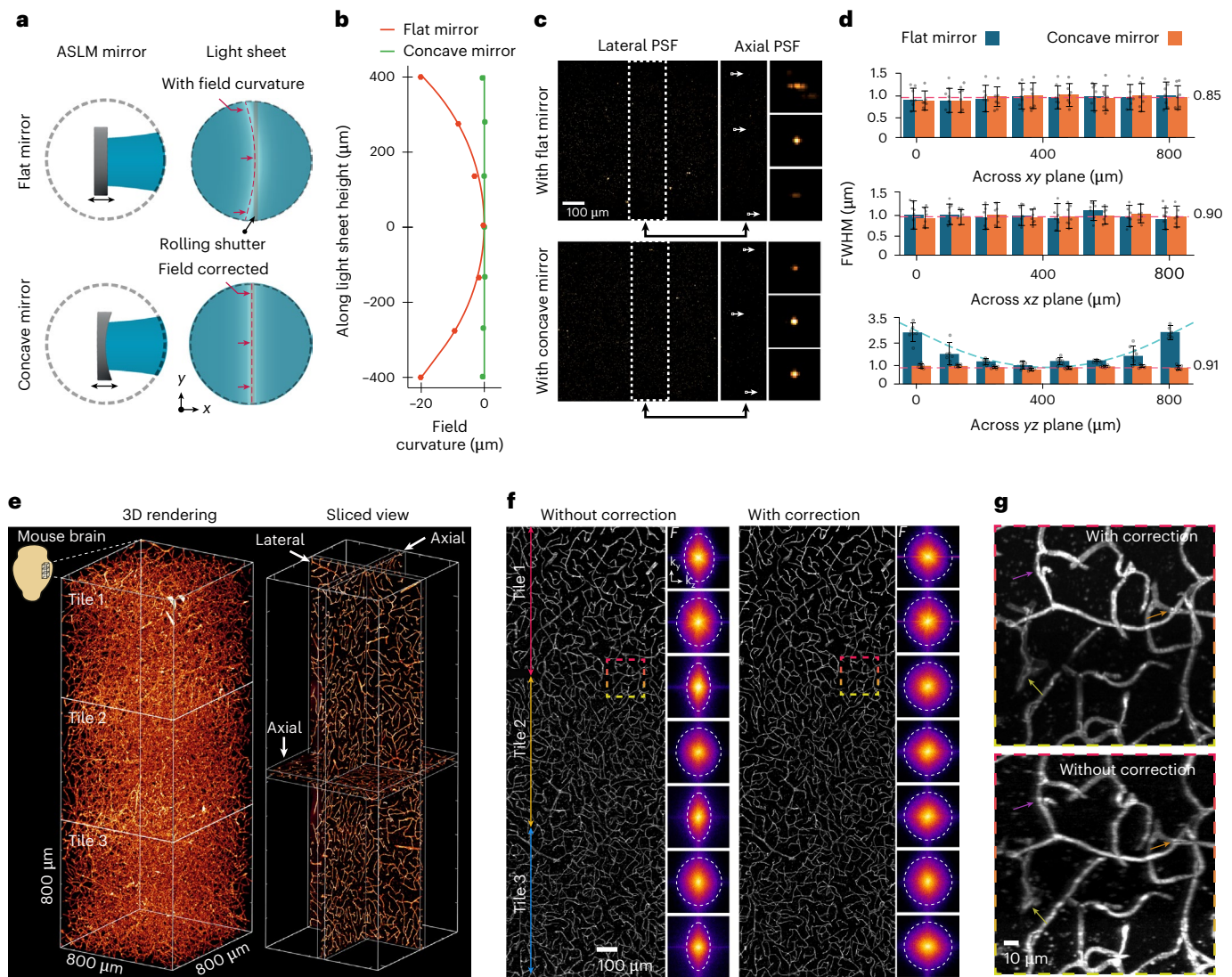


Fig. 2 | Flat-field-corrected light sheet enhances FOV and quality across the imaging tiles. **a**, Schematic comparison of using the flat mirror and curved mirror in the ASLM unit and their effect on the field curvature of the light sheet. **b**, Measured field curvature of the light sheet without (red) and with correction (green). **c,d**, PSF measurement with 200-nm nanoparticles and comparison without and with the field curvature correction in lateral and axial directions. The PSF FWHM (\pm s.e.m.) was measured for seven beads in each FOV section. **e**, 3D rendering and middle slices of the lateral and axial views of the recorded

data from a cleared mouse brain, stained for microvessels with three tiles along the height of the light sheet. The images are examples from one of three imaged mouse brains. **f**, Axial view of the recorded data in **d** along the light-sheet height and the corresponding Fourier domain comparison with its associated cut of frequency for seven regions. **g**, Enlarged view of selected areas in **f** located between adjacent tiles. The arrowheads show the improvements in vessel information with field curvature correction.

exposure time, recording it over the FOV from left to right (Fig. 1f and Supplementary Video 2).

Another essential requirement for ASLM is that the waist of the light sheet forms a straight line from top to bottom across the FOV. This is necessary to synchronize the thinnest part of the sweeping light sheet with the center of the rolling shutter. However, illumination field curvature is expected when using a high NA air objective lens in combination with high RI medium across a large FOV (Fig. 2a). To evaluate the illumination field curvature, we first imaged the light-sheet profile directly using a small mirror inside the chamber at 45 degrees between the optical arms. We then measured the center location of the light-sheet cross-section from top to bottom (Methods). The field curvature of the light sheet was $20 \pm 0.2 \mu\text{m}$ with an excitation beam of 561 nm and RI of 1.56, which was nearly three times larger than the light-sheet Rayleigh length (Fig. 2b, red line). To correct the light-sheet field curvature, we explored replacing the conventional flat mirror

in the ASLM unit with a concave mirror with an inverse curvature, as measured by the light-sheet field curvature. The chosen off-the-shelf concave mirror (CM127-010-P01, Thorlabs) has a 9.5-mm effective focal length with a maximum offset of 10 μm at 400 μm from its center, which covers the light sheet with an 800-μm height (Supplementary Fig. 4a). The field curvature was corrected to less than 1 μm along the light sheet (Fig. 2b, green line) compared to the flat mirror. Then, we characterized the axial resolution by imaging 200 nm nanoparticles and measuring the point spread function (PSF). When using the flat mirror, we measured a variety of axial PSFs over the light-sheet height from 800 nm to 2.5 μm (Fig. 2c). Here we achieved isotropic resolution only in the central 400 μm of the FOV, whereas the rest of the FOV remained nonisotropic. However, with the concave mirror, the axial resolution was homogeneous across the entire FOV, with an isotropic resolution of 850 nm. This enabled us to increase the effective FOV by a factor of two compared to the flat mirror (Fig. 2d).

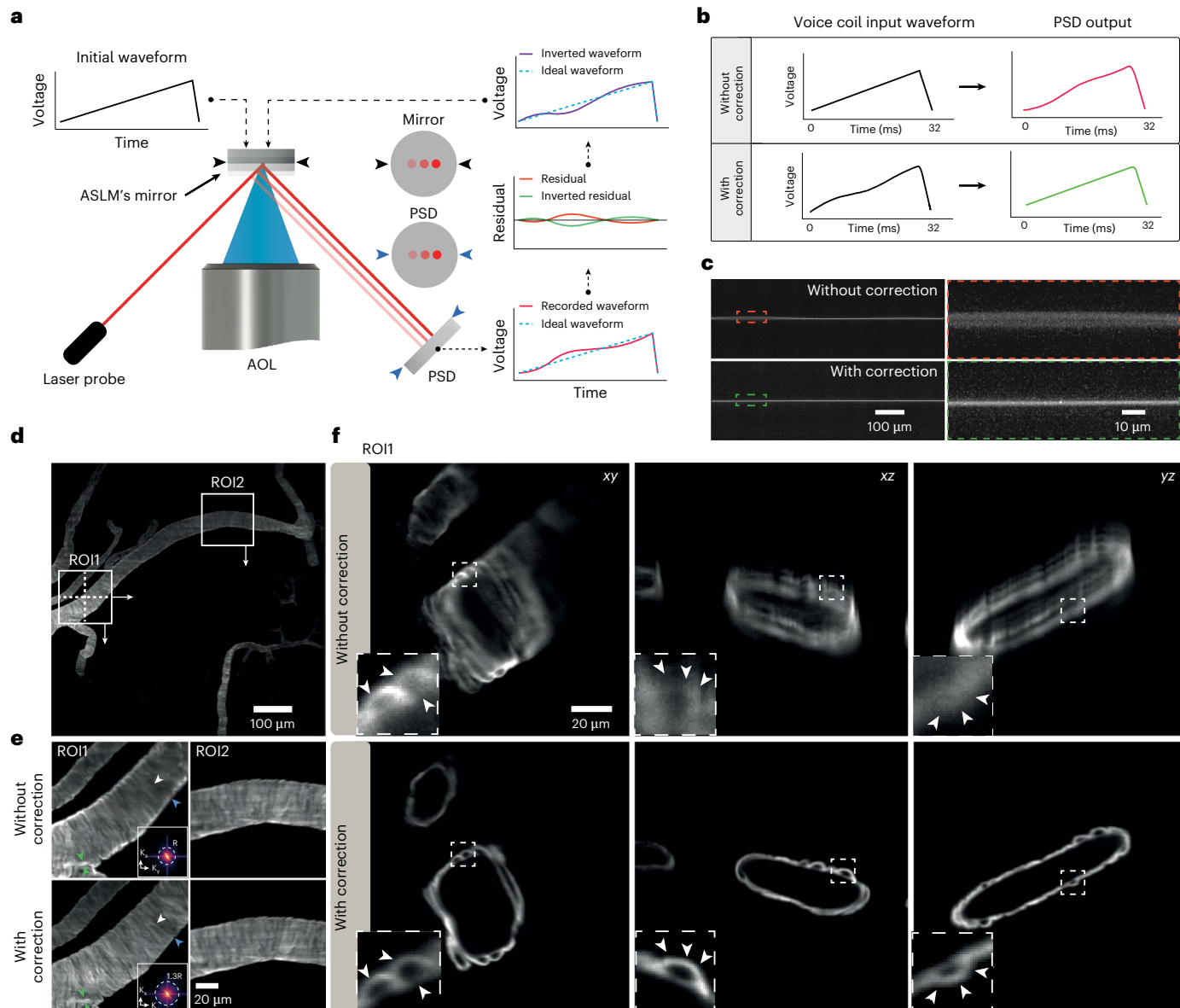


Fig. 3 | High-speed isotropic resolution achieved by voice coil waveform adaptation. **a**, Schematic of the PSD arrangement and the closed-loop control of the voice coil in the ASLM unit, along with the adaptive algorithm for correcting voice coil movement. PSD indicates the position-sensing device. **b**, Recorded feedback waveform from the PSD without and with correction at voice coil frequency 31 Hz. **c**, Recorded swept beam inside the chamber corresponding to the waveforms in **b** with an exposure time of 25 ms. **d**, Recorded mouse brain

stained for α SMA, showing a selected ROI with and without waveform correction. **e**, Selected ROI1 and ROI2 in **d**. Resolution analysis in the Fourier domain shows an increase in resolution after voice coil correction. **f**, Cross-section of ROI1 from **d** in the *xy*, *xz* and *yz* planes with and without voice coil movement correction. The subsets and arrowheads highlight the same area. The images in **d–f** are examples from one of four sampled images.

To examine the microscope's performance in cleared tissue, we used a mouse brain labeled with antibodies for brain endothelial cells, visualizing even the smallest vascular structures, so-called capillaries (Fig. 2e). The imaging was done for three tiles to evaluate the resolution across the volume, before and after field curvature correction (Fig. 2f). The axial view of the recorded images before field curvature correction showed that the cut-off frequency of the noncorrected images varied and decreased to almost half in the Fourier domain compared to the image with corrected field curvature. In contrast, image quality and the frequency distribution remained constant across the tiles when imaged with field curvature correction (Fig. 2g). Consequently, eliminating the light-sheet field curvature achieved isotropic resolution across a larger FOV and into the corners of the images, crucial for image stitching and quantitative imaging.

Alongside spatial resolution, imaging speed is also important for achieving high-throughput imaging of large samples. In ASLM, the maximum speed is determined mainly by the sweeping device, which in our case is a voice coil with a reported speed of up to only 10 Hz for ASLM¹³. To explore the voice coil's potential to move much faster, we developed a small, closed-loop monitoring arm with a low-power diode laser and a position-sensing detector (PSD; Fig. 3a). The axial movement of the voice coil translated into a lateral shift of the reflected laser on the PSD and a modulation of its voltage output (Methods). Our measurements across typical exposure times from 8 ms to 256 ms confirmed that the voice coil's response was not uniformly linear across all frequencies, particularly at higher frequencies, which desynchronized the movement of the light sheet and the rolling shutter at several parts of the FOV (Supplementary Fig. 5). To eliminate the nonuniformity,

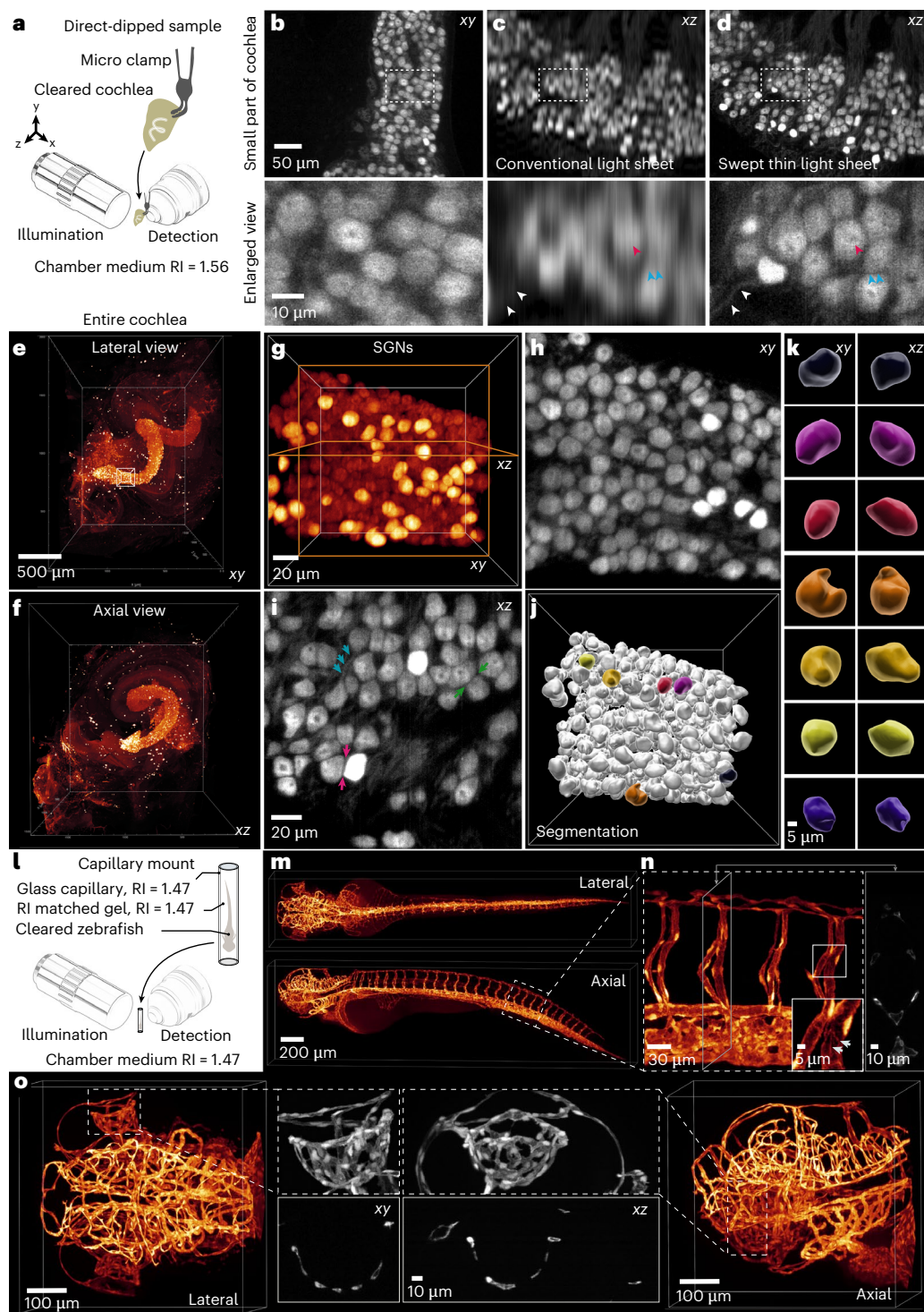


Fig. 4 | Imaging of a mouse cochlea with isotropic resolution. **a**, Schematic of the cochlea and its mounting in the microscope. **b**, Top: recorded data from a small section of an anti-PV-stained cochlea with a swept thin light sheet. Bottom: selected and magnified ROI from the top row. The image is an example from one of two imaged samples. **c**, Top: reconstructed axial image in **b** recorded with a conventional light sheet covering the entire FOV. Bottom: selected and magnified ROI from the top row. **d**, Top: reconstructed axial image in **b** recorded with a swept thin light sheet. Bottom: selected and magnified ROI from the top row. All arrows of the same color indicate comparisons between the magnified images in **c** and **d**. **e**, 3D reconstruction of a mouse cochlea from four tiles (lateral view). The image is an example from one of five imaged samples. **f**, 3D reconstruction of **e** (axial view). **g**, An ROI in the cochlea base with SGNs from **e**. **h,i**, Lateral (**h**) and axial (**i**) view of the midplane in **g**. Blue arrows mark

exemplary neurites of the bipolar SGNs. The green and red arrowheads indicate the well-resolved gap between the neurons due to the isotropic resolution. **j**, 3D rendering after segmentation in **g**. **k**, Selected segmented SGNs in **j** (lateral and axial view), labeled with a unique color for each SGN. **l**, Schematic of the zebrafish and its mounting in the microscope using a borosilicate glass capillary. **m**, 3D reconstruction of the zebrafish from both lateral and axial views. The image is an example from one of four imaged samples. **n**, Enlarged view of a selected ROI in the tail; the inset highlights magnified vessels within this ROI. All arrows indicate the endothelial cell boundaries. The right panel displays a cross-section of the tail. **o**, Enlarged views of the zebrafish head from **m**, including lateral and axial views (first and last). The middle images represent maximum intensity projections of the vasculature around the eye in both orientations, along with a central cross-section.

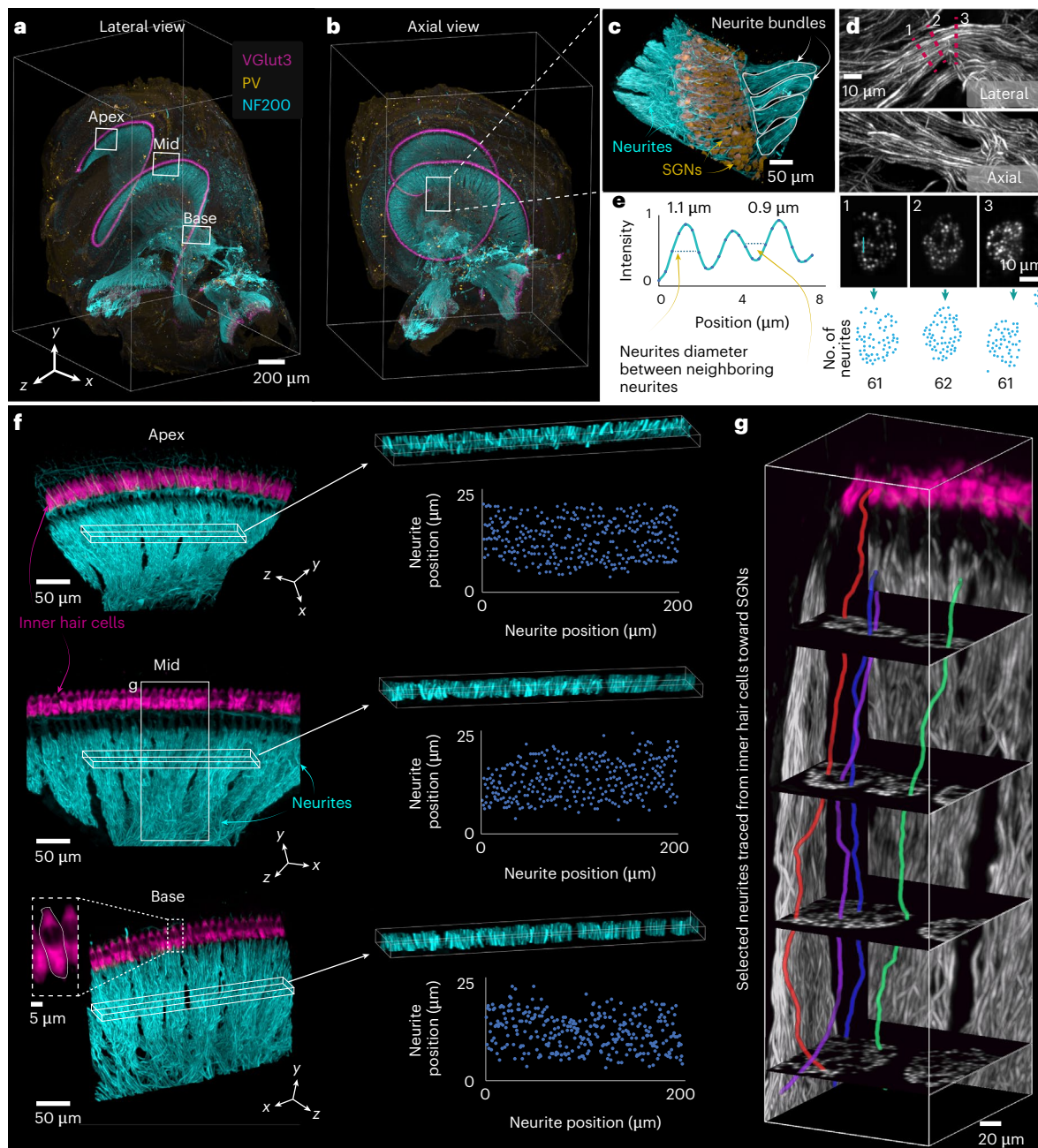


Fig. 5 | Multicolor imaging of the mouse cochlea. **a, b**, Lateral (a) and axial (b) views of a full cochlea volume showing IHCs immunolabeled for VGlut3, SGNs labeled with anti-PV and neurites labeled with NF200 in x, y and z. The image is an example from one of three imaged samples. **c**, Selected and magnified ROI from b, showing neurites and SGNs (left) and neurites in lateral and axial views (right). **d**, Analysis of a single neurite bundle in c. First row: lateral view; second row: axial view; third row: neurite diameter and position in three oblique planes along the neurite extension marked with a red dashed line and numbered 1, 2, 3; fourth row: neurite count from exemplary cross-sections shown in d, first row. **e**, Line profile of three neighboring neurites in cross-section 3 in d. **f**, Selected ROIs from the apical, middle and basal turns of the cochlea, as shown in a, depicting IHCs labeled with VGlut3 and neurites labeled with NF200 to visualize neurite positions for exemplary counting across all cochlear turns. **g**, Tracing SGN neurites from the organ of Corti to the spiral ganglion in an ROI from the midturn of the cochlea, shown in d.

fourth row: neurite count from exemplary cross-sections shown in d, first row. **e**, Line profile of three neighboring neurites in cross-section 3 in d. **f**, Selected ROIs from the apical, middle and basal turns of the cochlea, as shown in a, depicting IHCs labeled with VGlut3 and neurites labeled with NF200 to visualize neurite positions for exemplary counting across all cochlear turns. **g**, Tracing SGN neurites from the organ of Corti to the spiral ganglion in an ROI from the midturn of the cochlea, shown in d.

a correction waveform was calculated based on the residual of the voice coil's response to the initial sawtooth waveform, which was then applied back on the voice coil as a correction waveform. Notably, even after just a few iteration cycles, the voice coil's movement became uniformly linear, allowing for precise synchronization between the sweeping light sheet and the sCMOS rolling shutter at almost full speed without compromising FOV coverage (Fig. 3b,c). This approach also allowed us to synchronize the voice coil with the rolling shutter at a frame rate of 100 frames per second (fps) (Supplementary Table 1).

We next tested the system's performance for high spatiotemporal resolution imaging of a piece of cleared mouse brain (800 μ m \times 800 μ m \times 2,400 μ m) with fluorescently labeled larger vessels, especially arteries and arterioles, using an antibody detecting smooth muscle cells (α -smooth muscle actin, α SMA; Fig. 3d). Here, the imaging was done with an sCMOS camera with a controllable rolling shutter at its maximum frame rate (PCO Panda; Supplementary Table 1). The recorded data showed a resolution variation across the FOV and along the sweeping light sheet in both lateral and axial views before the voice

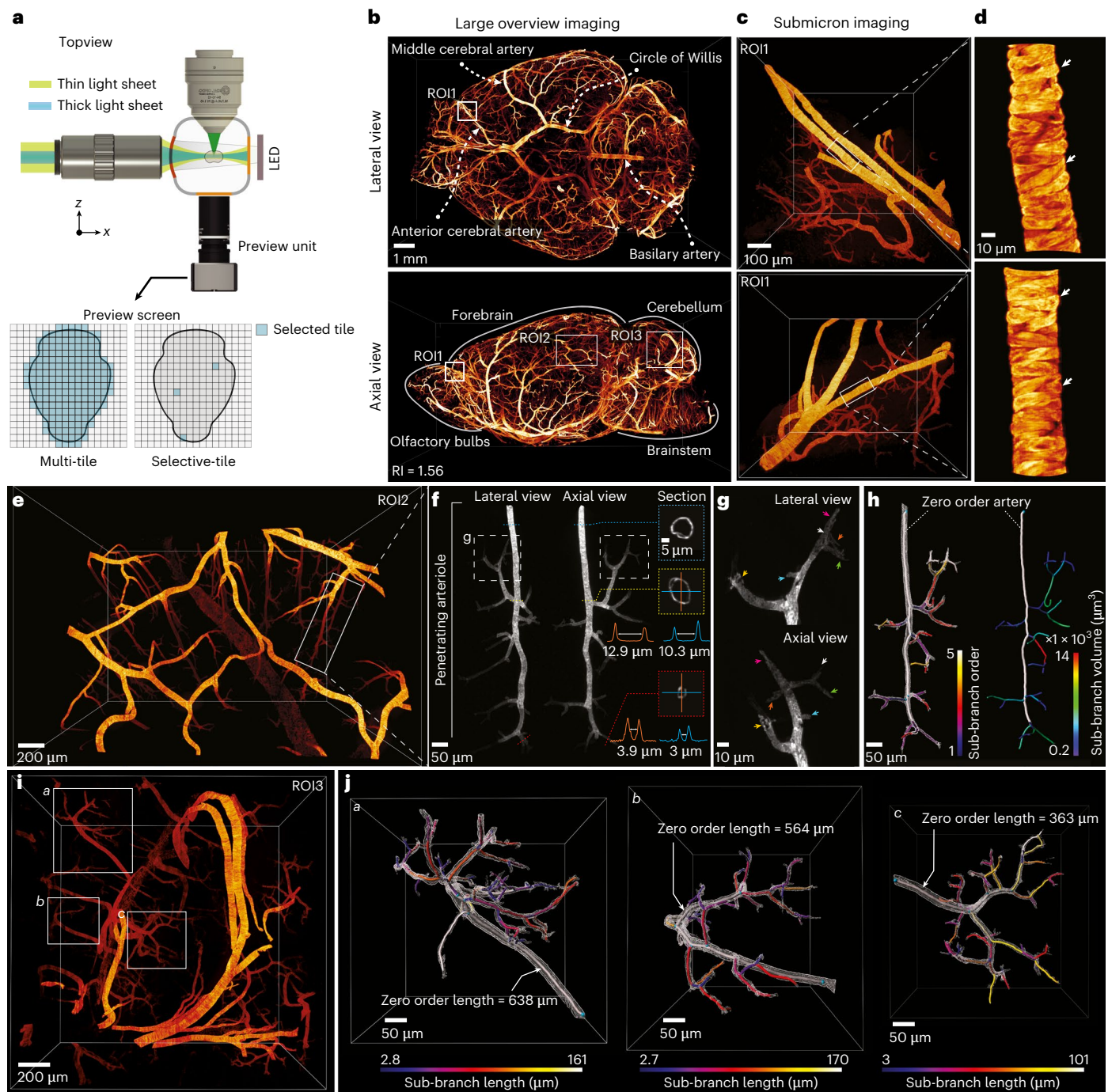


Fig. 6 | Hybrid imaging of an entire cleared mouse brain. **a**, Schematic of the setup with chamber, lenses and a small camera unit for capturing a preview image of a large sample and selecting the tiles. **b**, Entire reconstructed mouse brain from lateral and axial views. The image is an example from one of two imaged samples. **c**, Re-imaged selected ROI in **b** and the reconstructed axial view (second row). **d**, Enlarged view of selected small vessel in **c** (first row) and reconstructed axial view (second row), highlighting individual vessel cells (arrowheads). **e**, Selected ROI2 from the cortex in **b**, which was recorded with the highest possible isotropic resolution. The image is an example from one of two imaged samples. **f**, Selected penetrating arteriole and cross-sections at different depths and branches. The vertical line (orange solid line) and horizontal line (blue solid line) profiles indicate the measured line profiles from the cross-sections

of the zero-order artery and the last SMA-positive termini. The inner distance between the artery walls was measured and indicated with a white double arrowhead line. **g**, Enlarged view of one of the penetrating subarteries in **f**. The color-coded arrowheads indicate the last SMA-positive arterial termini with the same color from both lateral and axial views. **h**, Left: segmentation of the entire penetrating artery and the counted sub-branches until the last SMA-positive termini. Right, the calculated volume of the main and subarteries. **i**, Selected ROI3 from the cerebellum in **b**, which was recorded with the highest possible isotropic resolution. The image is an example from one of two imaged samples. **j**, Full segmentation of three selected penetrating arteries named *a*, *b* and *c*. The segmentation and artery tracing enabled us to find the length of the main and subarteries in all directions.

coil waveform correction. Notably, the isotropic resolution across the entire FOV was achieved only with the corrected waveform of the voice coil. Individual fine vasculature structures were resolved in all directions at submicron scale at 40 Hz across the entire FOV (Fig. 3e,f).

Benchmarking the light-sheet system by imaging cleared specimens at different RIs

To benchmark the microscope's performance for rapid and isotropic imaging of whole cleared organ samples, we first imaged an entire mouse cochlea. The cochlea offers an intricate snail-shaped three-dimensional (3D) structure with the spiral ganglion sampling sound information along the frequency axis. iDisco cleared mouse cochlea¹⁰ (Methods) were matched with an RI of 1.56 (ECi; Fig. 4a). Immunolabeling with parvalbumin (PV) allows for robust visualization of the entire population of spiral ganglion neurons (SGNs) within the Rosenthal canal. We first imaged a small part of the cochlea to see how much more information can be retrieved along the axial direction when using a thin swept light sheet compared to a conventional light sheet with a thickness of about 5 μm covering the entire FOV: detailed observation, especially in the axial direction, had hitherto remained elusive when using conventional light-sheet methods (Fig. 4b–d). The typical volume of a cochlea is approximately 1.5 mm \times 1.5 mm \times 2 mm (Fig. 4e,f) and could be imaged in four tiles. We employed a plane spacing of 380 nm, consistent with the pixel size, for an RI of 1.56 to achieve a resolution of 850 nm. Up to 4,000 imaging planes were needed in each tile to cover the entire volume. Because of the isotropic resolution, each SGN was clearly distinguished from its neighbors, and neurites were detected (Fig. 4g–i), enabling us to segment each SGN properly (Fig. 4j,k). Alongside submicron isotropic resolution, our microscope allowed us to image a mouse cochlea with four tiles in just 2.1 to 8.5 min at an exposure time of just 8–32 ms, respectively (Supplementary Video 3).

To evaluate the microscope's performance at different RIs, we cleared a 3 days postfertilization (dpf) Tg(kdrl:GFP) zebrafish using an adjusted version of the EZ Clear protocol²⁰ (Methods). The zebrafish was mounted in an RI-matched agarose gel (RI = 1.47) inside a borosilicate glass capillary suspended in glycerol (Fig. 4l). This mounting method allows for easy mounting of delicate or fragile samples while maintaining a uniform RI (Methods). The sample was imaged in four tiles, totaling 8,000 planes for the entire sample, with a plane spacing of 390 nm. The entire sample is recorded with 100 fps within an acquisition time of 1 min and 20 s (Fig. 4m–o). The data showed consistent image quality in both lateral and axial views, with fine details such as endothelial cell boundaries clearly resolved in all directions (inset; Fig. 4n). Isotropic resolution was confirmed by examining the delicate ophthalmic vasculature in both lateral and axial views, which showed equally well-resolved vascular walls and lumina (Fig. 4o and Supplementary Video 4).

Isotropic 3D imaging enables analysis of cochlear connectomics

To demonstrate the biological applicability and resolution performance of our light-sheet microscope in structured and functionally critical tissue, we performed high-resolution imaging of cochlear afferent innervation. Using triple-color fluorescent labeling, we visualized inner hair cells (IHCs), SGNs and their peripheral neurites (Fig. 5a,b). Imaging was carried out at the system's maximum isotropic resolution, enabling a comprehensive 3D reconstruction of cochlear architecture with consistent detail across all spatial orientations. We first rendered whole-organ 3D overviews with clearly separated channels, followed by the selection of a region of interest (ROI) from the basal turn encompassing SGNs and their neurites (Fig. 5c–e and Supplementary Video 5). Within this ROI, we extracted three cross-sectional planes perpendicular to the local neurite trajectory at distinct locations along the cochlear spiral. In these planes, individual neurites could be resolved and

counted, indicating that fine anatomical structures remained sharply defined regardless of orientation. This underscores the system's isotropic resolution and its suitability for neuroanatomical quantification.

To expand the analysis, we selected three larger ROIs from the apical, middle and basal turns. In each, we quantified the number of SGN neurites terminating on 25 adjacent IHCs—a direct proxy for IHC–SGN connectivity, which is critical for understanding auditory function and pathology (Fig. 5f). The ability to perform these counts across the cochlea consistently reflects the uniform image quality, enabling comparative assessments of innervation density and spatial patterning along the tonotopic axis.

We then traced and segmented selected neurites from their synaptic connection with IHCs to the corresponding SGN soma within the Rosenthal's canal, capturing their full 3D trajectories (Fig. 5g). This level of structural detail supports studies of cochlear neuronal connectivity, allowing reconstruction and analysis of afferent pathways at the single-cell level. Such detailed mapping opens the door to systematic studies of cochlear connectomics, including afferent synaptic organization of type I and II SGNs, molecularly defined type I SGN subtypes^{29–31}, efferent connectivity, and circuit-level remodeling in health and disease.

Imaging of the whole mouse brain

To assess the system's performance in imaging even larger specimens, we imaged an entire mouse brain (14 mm \times 10 mm \times 7 mm) immunolabeled for arteries and arterioles by α SMA-targeting antibodies (Supplementary Fig. 6; Methods). A compact preview system with a \times 0.3 optical magnification was installed opposite the detection lens, providing a large overview of approximately 15 mm \times 15 mm (Fig. 6a). The preview assists the user in choosing the desired orientation and selecting several tiles across the entire sample, each covering a full detection FOV of 800 μm \times 800 μm .

We first acquired a quick overview of the mouse brain by selecting all the tiles covering the brain and imaging them with a thick light sheet (3.8 μm). This reduction in axial resolution is achieved quickly by limiting the NA of the illumination beam with an adjustable slit. To achieve an isotropic overview, the pixel size of the recorded image was then matched to the light-sheet thickness by a binning of ten. The entire mouse brain was recorded and reconstructed at this resolution in less than 30 min. The reconstructed data enabled us to identify the entire brain's vasculature trees, including the main arteries located at the surface as well as deeper arterioles (Fig. 6b). To observe the vessels' subcellular structure, we identified ROIs, for example, part of the anterior cerebral artery, and re-imaged the related selected tile volume (800 μm \times 800 μm \times 800 μm) again at the highest possible isotropic resolution (850 nm), which only took about 21 s for 2,100 layers (Fig. 6c). The raw data provided isotropic subcellular information of individual smooth muscle cells viewed from any angle without deconvolution or other processing (Fig. 6d and Supplementary Video 6).

To further benchmark the biological relevance and resolution fidelity of the system, we imaged two distinct parts of the mouse brain, targeting anatomically and functionally different regions: the cerebral cortex and the cerebellum. Imaging was carried out at the maximum achievable resolution, allowing us to visualize fine vascular structures throughout the entire volume without compromising depth or FOV. In each region, we isolated and analyzed three individual penetrating arteries, each differing in depth and spatial orientation. We were able to accurately measure vessel diameter along their full trajectories, regardless of spatial orientation or local deformation—demonstrating the system's ability to maintain uniform, isotropic resolution. This overcomes a main limitation of conventional LSFM systems, which often suffer from degraded axial resolution (Fig. 6e,f).

Using 3D segmentation and skeletonization, we reconstructed the full branching architecture of each vessel down to the last SMA-positive termini (Fig. 6g). Precise illustration of the arteriolar-capillary

transition zone allowed for clear distinction of different types of mural cells without additional markers or tissue cutting. The ring-like morphology of smooth muscle cells in the arterioles was replaced by an enwrapping morphology in higher-order vessels, reflecting ensheathing pericytes³². Notably, mural cells in higher-order branches appeared less intense, suggesting a reduced expression of α SMA in those cells. The full reconstruction enabled precise quantification of branch number, length and morphology (Fig. 6h and Supplementary Fig. 7), supporting applications that rely on high-fidelity structural analysis, such as vascular remodeling, angiogenesis during development or vascular remodeling after ischemic insults.

In the cerebellum, vascular features—including the lengths of penetrating arterioles, branching patterns and compact geometries—were also readily recorded. These characteristics, which differ from those in the cortex and reflect the anatomical and functional distinctions of this brain region, were visualized without the need for angle-specific imaging, highlighting the versatility and consistency of our system (Fig. 6i,j).

Overall, this analysis highlights how our microscope enables orientation-independent, subcellular-resolution imaging across large tissue volumes. The ability to accurately trace and quantify individual vessels in three dimensions, regardless of geometry or orientation, makes it a powerful tool for investigating brain vasculature, microcirculation and disease-associated structural changes at unprecedented clarity and scale.

Discussion

High-resolution 3D imaging and quantitative analysis of large biological samples are essential for understanding complex structures such as neuronal circuits and vascular networks. Maintaining spatial context throughout the entire volumes allows for precise and efficient extraction of morphological and functional insights. To meet these needs, we have developed a rapid, aberration-corrected light-sheet microscope for imaging cleared tissues with isotropic submicron resolution. This approach demonstrates that detailed morphometric and connectivity analysis across whole specimens has now become possible without requiring tissue reorientation, flattening, distortion or sectioning.

The microscope uses an axially swept light sheet to achieve isotropic resolution over a large FOV. We found that the light-sheet field curvature can be effectively corrected by replacing the flat mirror in the ASLM with an off-the-shelf concave mirror rather than using an expensive, dedicated objective lens. The straightened light sheet is key to achieving an isotropic PSF across the extended FOV and stitching volume tiles accurately. Although we have corrected the field curvature only in our illumination arm, the same principle could be extended to remote focusing in the detection arm for fast volumetric imaging, as sometimes required in live imaging.

Furthermore, we minimized spherical aberrations and achieved a near-diffraction-limited light sheet using identical, easily exchangeable high NA air objective lenses in both the illumination and ASLM arm. Combined with an off-the-shelf meniscus lens, we achieved submicron resolution. Aberrations in the illumination arm are minimized because both objective lenses are identical. Again, this concept represents a cost-effective solution that could also be extended to the detection arm in future developments. The curvature of the meniscus lens is chosen to match our primary NA of 0.4, but can be adapted to other lenses as needed.

Our closed-loop technique for calibrating and monitoring the ASLM unit enables us to achieve the very high frame rate of 100 Hz. The system controls several aspects of operation, such as precalibrating the voice coil's running waveform and monitoring the voice coil's movement for any drift, for example, due to environmental factors such as temperature. Our technique can adapt to various voice coil frequencies, such as the typical sCMOS with 40 Hz, 100 Hz and 122 Hz frame rates in light-sheet mode (Supplementary Table 1), making it universally applicable and robust. Further advancements in sCMOS

technology with additional light-sheet modes and potentially higher frame rates can be incorporated without sacrificing FOV. Furthermore, our approach may apply to other microscopy techniques that rely on precise remote focusing³³.

The striping artifacts typically associated with light-sheet microscopy are less pronounced when samples are well-cleared and RI-matched as shown. However, residual striping artifacts can be mitigated using multidirectional selective plane illumination microscopy (mSPIM)³⁴ or computational methods³⁵. The mSPIM could be integrated seamlessly into our microscope by employing a fast resonance mirror or an acousto-optic deflector (AOD) with kilohertz-level scanning. Nevertheless, some samples may not achieve perfect RI matching due to hard tissues like bone³⁶, which may shift the light sheet and detection plane from the perfect focus³⁷. We have addressed this issue by axially fine-tuning the light-sheet position through voice coil offset adjustments and defocusing the light sheet to the detection plane using a motorized mirror placed after the CL. Finding the optimal imaging angle may become important in future developments, potentially leveraging smart rotation³⁸. Although our proposed method has been applied within a conventional light-sheet configuration with two objective lenses, all techniques introduced in this study can be adapted readily to various other light-sheet configurations with different numbers of lenses for diverse applications, including live tissue imaging.

In summary, our cleared tissue microscope is a robust, compact system built from commercially available, off-the-shelf components. We achieved isotropic, submicron resolution in all directions with high-speed imaging for high-throughput imaging of biological samples. Our light-sheet microscope can reveal the complex subcellular architecture across large intact tissues, providing new insights for biological and medical research.

Online content

Any methods, additional references, Nature Portfolio reporting summaries, source data, extended data, supplementary information, acknowledgements, peer review information; details of author contributions and competing interests; and statements of data and code availability are available at <https://doi.org/10.1038/s41587-025-02882-8>.

References

1. Huisken, J., Swoger, J., Del Bene, F., Wittbrodt, J. & Stelzer, E. H. K. Optical sectioning deep inside live embryos by selective plane illumination microscopy. *Science* **305**, 1007–1009 (2004).
2. Keller, P. J., Schmidt, A. D., Wittbrodt, J. & Stelzer, E. H. K. Reconstruction of zebrafish early embryonic development by scanned light sheet microscopy. *Science* **322**, 1065–1069 (2008).
3. Huisken, J. & Stainier, D. Y. R. Selective plane illumination microscopy techniques in developmental biology. *Development* **136**, 1963–1975 (2009).
4. Krzic, U., Gunther, S., Saunders, T. E., Streichan, S. J. & Hufnagel, L. Multiview light-sheet microscope for rapid *in toto* imaging. *Nat. Methods* **9**, 730–733 (2012).
5. Engelbrecht, C. J. & Stelzer, E. H. Resolution enhancement in a light-sheet-based microscope (SPIM). *Opt. Lett.* **31**, 1477 (2006).
6. Dodt, H.-U. et al. Ultramicroscopy: three-dimensional visualization of neuronal networks in the whole mouse brain. *Nat. Methods* **4**, 331–336 (2007).
7. Tomer, R., Ye, L., Hsueh, B. & Deisseroth, K. Advanced CLARITY for rapid and high-resolution imaging of intact tissues. *Nat. Protoc.* **9**, 1682–1697 (2014).
8. Stefaniuk, M. et al. Light-sheet microscopy imaging of a whole cleared rat brain with Thy1-GFP transgene. *Sci. Rep.* **6**, 28209 (2016).
9. Pende, M. et al. High-resolution ultramicroscopy of the developing and adult nervous system in optically cleared *Drosophila melanogaster*. *Nat. Commun.* **9**, 4731 (2018).

10. Keppeler, D. et al. Multiscale photonic imaging of the native and implanted cochlea. *Proc. Natl Acad. Sci. USA* **118**, e2014472118 (2021).
11. Power, R. M. & Huisken, J. A guide to light-sheet fluorescence microscopy for multiscale imaging. *Nat. Methods* **14**, 360–373 (2017).
12. Dean, K. M., Roudot, P., Welf, E. S., Danuser, G. & Fiolka, R. Deconvolution-free subcellular imaging with axially swept light sheet microscopy. *Biophys. J.* **108**, 2807–2815 (2015).
13. Chakraborty, T. et al. Light-sheet microscopy of cleared tissues with isotropic, subcellular resolution. *Nat. Methods* **16**, 1109–1113 (2019).
14. Voigt, F. F. et al. The mesoSPIM initiative: open-source light-sheet microscopes for imaging cleared tissue. *Nat. Methods* **16**, 1105–1108 (2019).
15. Vladimirov, N. et al. Benchtop mesoSPIM: a next-generation open-source light-sheet microscope for cleared samples. *Nat. Commun.* **15**, 2679 (2024).
16. Chen, F., Tillberg, P. W. & Boyden, E. S. Expansion microscopy. *Science* **347**, 543–548 (2015).
17. Wassie, A. T., Zhao, Y. & Boyden, E. S. Expansion microscopy: principles and uses in biological research. *Nat. Methods* **16**, 33–41 (2019).
18. Ertürk, A. et al. Three-dimensional imaging of solvent-cleared organs using 3DISCO. *Nat. Protoc.* **7**, 1983–1995 (2012).
19. Renier, N. et al. iDISCO: a simple, rapid method to immunolabel large tissue samples for volume imaging. *Cell* **159**, 896–910 (2014).
20. Hsu, C.-W. et al. EZ Clear for simple, rapid, and robust mouse whole organ clearing. *eLife* **11**, e77419 (2022).
21. Chen, Y. et al. Low-cost and scalable projected light-sheet microscopy for the high-resolution imaging of cleared tissue and living samples. *Nat. Biomed. Eng.* **8**, 1109–1123 (2024).
22. Otomo, K. et al. descSPIM: an affordable and easy-to-build light-sheet microscope optimized for tissue clearing techniques. *Nat. Commun.* **15**, 4941 (2024).
23. Barner, L. A., Glaser, A. K., True, L. D., Reder, N. P. & Liu, J. T. C. Solid immersion meniscus lens (SIMlens) for open-top light-sheet microscopy. *Opt. Lett.* **44**, 4451 (2019).
24. Glaser, A. K. et al. A hybrid open-top light-sheet microscope for versatile multi-scale imaging of cleared tissues. *Nat. Methods* **19**, 613–619 (2022).
25. Bishop, K. W. et al. Axially swept open-top light-sheet microscopy for densely labeled clinical specimens. *Opt. Lett.* **49**, 3794 (2024).
26. Zhang, Y. & Gross, H. Systematic design of microscope objectives. Part I: system review and analysis. *Adv. Opt. Technol.* **8**, 313–347 (2019).
27. Glaser, A. et al. Expansion-assisted selective plane illumination microscopy for nanoscale imaging of centimeter-scale tissues. *eLife* **12**, RP91979 (2025).
28. Tang, L. et al. Curved light sheet microscopy for centimeter-scale cleared tissues imaging. *Nat. Photonics* **19**, 577–584 (2025).
29. Petitpré, C. et al. Neuronal heterogeneity and stereotyped connectivity in the auditory afferent system. *Nat. Commun.* **9**, 3691 (2018).
30. Sun, S. et al. Hair cell mechanotransduction regulates spontaneous activity and spiral ganglion subtype specification in the auditory system. *Cell* **174**, 1247–1263 (2018).
31. Shrestha, B. R. et al. Sensory neuron diversity in the inner ear is shaped by activity. *Cell* **174**, 1229–1246 (2018).
32. Grant, R. I. et al. Organizational hierarchy and structural diversity of microvascular pericytes in adult mouse cortex. *J. Cereb. Blood Flow. Metab.* **39**, 411–425 (2019).
33. Sofroniew, N. J., Flickinger, D., King, J. & Svoboda, K. A large field of view two-photon mesoscope with subcellular resolution for *in vivo* imaging. *eLife* **5**, e14472 (2016).
34. Huisken, J. & Stainier, D. Y. R. Even fluorescence excitation by multidirectional selective plane illumination microscopy (mSPIM). *Opt. Lett.* **32**, 2608 (2007).
35. Peng, T. et al. Leonardo: a toolset to remove sample-induced aberrations in light sheet microscopy images. Preprint at Research Square <https://www.researchsquare.com/article/rs-5853941/v1> (2025).
36. Weiss, K. R., Voigt, F. F., Shepherd, D. P. & Huisken, J. Tutorial: practical considerations for tissue clearing and imaging. *Nat. Protoc.* **16**, 2732–2748 (2021).
37. Ryan, D. P. et al. Automatic and adaptive heterogeneous refractive index compensation for light-sheet microscopy. *Nat. Commun.* **8**, 612 (2017).
38. He, J. & Huisken, J. Image quality guided smart rotation improves coverage in microscopy. *Nat. Commun.* **11**, 150 (2020).

Publisher's note Springer Nature remains neutral with regard to jurisdictional claims in published maps and institutional affiliations.

Open Access This article is licensed under a Creative Commons Attribution 4.0 International License, which permits use, sharing, adaptation, distribution and reproduction in any medium or format, as long as you give appropriate credit to the original author(s) and the source, provide a link to the Creative Commons licence, and indicate if changes were made. The images or other third party material in this article are included in the article's Creative Commons licence, unless indicated otherwise in a credit line to the material. If material is not included in the article's Creative Commons licence and your intended use is not permitted by statutory regulation or exceeds the permitted use, you will need to obtain permission directly from the copyright holder. To view a copy of this licence, visit <http://creativecommons.org/licenses/by/4.0/>.

© The Author(s) 2025

Methods

Optical setup

The optical setup consists of six units: laser launch, remote focusing, illumination arm, chamber, detection arm and preview unit.

- (1) **Laser launch:** the setup can either be used with a fiber-beam laser engine (CLE laser engine, 20 mW each laser line, TOP-TICA) or a free-beam laser engine (OBISCellX, 100 mW each laser line, Coherent). Each laser engine provides four laser lines at 405 nm, 488 nm, 561 nm and 640 nm. When using a fiber-coupled laser, the laser beam is collimated with a 25-mm lens, which gives a 7-mm beam. For the free laser beam, a lens with $f = 50$ mm lens (where f denotes the focal length) is paired with a lens with $f = 25$ mm to provide a twofold beam expansion, which also provides a beam with a 7-mm diameter at the 561-nm laser line. Following the beam collimation and expansion, an initial light sheet is formed with a CL with $f = 45$ mm. This primary light sheet is subsequently collected by a secondary lens with $f = 60$ mm. A polarizing beam splitter (PBS) that guides the beam through the ASLM arm is positioned in front of this secondary lens.
- (2) **Remote focusing:** the beam polarization is controlled by rotating the optical fiber to achieve maximum reflection at the PBS toward the ASLM. After passing the PBS, the laser beam encounters a sequence of optical elements: a quarter-wave plate (QWP), a 100-mm lens, a mirror, and a $\times 20$ objective lens before hitting the ASLM mirror. The QWP converts the laser beam's linear polarization into circular polarization (for example, clockwise). After reflection from the ASLM mirror, the beam returns with a circular polarization in the opposite direction (counterclockwise). When the beam passes through the QWP again, it regains linear polarization but in an orthogonal direction, enabling it to pass through the PBS and proceed to the IL. The ASLM unit has a voice coil actuator (Thorlabs Blink) to sweep the light sheet. This setup includes either a flat mirror with a diameter of 12.5 mm (Thorlabs) or a concave mirror (Thorlabs, cat. no. CM127-010-P01) with a 9.5-mm focal length, which corrects the light-sheet field curvature while simultaneously sweeping the light sheet.
- (3) **Illumination arm:** following the PBS toward the main illumination arm, a 60-mm focal length lens collects the reflected beam after the remote focusing. The lens back focal plane is conjugated to the PBS center, while its front focal plane aligns with the IL back focal plane (Mitutoyo $\times 20$ NA 0.4, cat. no. MY20X-804). After the illumination lens, the beam encounters a positive meniscus lens with a 100-mm focal length (Thorlabs, cat. no. LE1234). This lens acts as a correction plate, preventing spherical aberrations when transitioning from air to a medium with a higher RI in the chamber.
- (4) **Chamber:** the chamber is made out of aluminum with four openings. One is used for holding the meniscus lens (Thorlabs, cat. no. LE1234). Two of them hold two glass windows with a thickness of 1 mm (Thorlabs, cat. no. WG10110), one for the preview camera and one for the preview LED. The last opening is used for the dipping detection objective lens. All the glass and lenses are sealed with sealant O-rings.
- (5) **Detection unit:** the detection unit uses a multi-immersion dipping objective lens (ASI multi-immersion lens $\times 16$ NA 0.4, 15-10-12) with a working distance of 12 mm at RI 1.45. The emission light is filtered through one of the six emission filters mounted on a custom-made filter wheel equipped with a robotic servomotor. For standard operation, the image is formed by a 200 mm TL (Thorlabs, cat. no. TTL200-A) onto an sCMOS chip with a rolling shutter (PCO Panda 4.2.m or Hamamatsu Fusion, cat. no. C14440-20UP) featuring a 6.5- μ m pixel size and

a 2,048 \times 2,048 pixel square chip. Alternatively, a 160-mm tube lens was used for an sCMOS chip with a 4.6- μ m pixel size (PCO 10bi CLHS).

- (6) **Stage and sample holder:** for volumetric imaging, the specimen is moved continuously through the light sheet in the z direction. This process captures a block tile using a linear stage (PI M112) at plane spacings of 0.38 μ m, mirroring the detection system pixel size, when the RI is at 1.56. Here we used tiles in the x and y dimensions for specimens that exceed the detection system's FOV, using another two linear stages (PI M112).

RI compatibility

The meniscus lens (positive meniscus, focal length 100 mm) was selected to match the curvature of the illumination beam's wavefront, which is determined by the NA of the illumination objective. This design ensured that the beam enters the sample chamber from air into higher RI media at a nearly perpendicular angle across the entire beam profile. Consequently, the performance of the meniscus lens remained unaffected by the RI of the chamber medium, making it compatible with all common clearing protocols. Similarly, the concave mirror used in the ASLM path compensated for the field curvature introduced by the overall optical setup of the illumination arm. Its function is also independent of the chamber RI. Therefore, switching between different immersion media requires no replacement of the meniscus lens or the concave mirror.

Compensation of chromatic aberrations for multiwavelength imaging

We used an air objective lens in the illumination arm, which, in combination with the high RI of the clearing solvent, can introduce chromatic aberrations. This resulted in wavelength-dependent shifts in the position of the light sheet along the sweeping direction. To correct for this shift and ensure that all wavelengths focus at the same position, we experimentally determined the optimal offset voltage for the voice coil actuator at each excitation wavelength. As we performed multicolor imaging sequentially, we loaded a separate, precalibrated waveform for each laser wavelength, each with the appropriate offset voltage applied. This ensured that light sheets of different wavelengths are aligned spatially with the rolling shutter, enabling accurate multicolor imaging without chromatic aberration.

Data streaming, postprocessing and visualization

The microscope is operated by a compact computer (NUC 11) running on an Ubuntu operating system. The data collected by the sCMOS is streamed seamlessly from the NUC to an external solid-state drive (Samsung T7, 4TB) via a Thunderbolt connection during standard operations, maintaining a frame rate of under 40 fps. For higher frame rates exceeding 40 fps, a 2TB M2 (Samsung NVMe) drive housed in an enclosure that supports Thunderbolt 4 is used, allowing for a streaming speed of 40 Gb per second. Each imaged volume tile is stacked directly in BigTiff or RAW format as it is written to the external solid-state drive. Subsequently, the data is converted into HDF5 format to enable lossless compression for Fiji³⁹ (v.1.54p) and BigStitcher⁴⁰ (v.2.5.2) for further analysis and image stitching. All 3D rendering and segmentation have been done using Imaris (v.9.7).

PSF measurement

The microscope's PSF was measured by imaging 200-nm gold nanoparticles (Aldrich, cat. no. 742066, lot no. MKCQ8675) embedded in clear, RI-matched agarose gel. First, 1.5% hard-gelling agarose is prepared with 0.2% gold nanoparticles already vortexed for about 5 min to avoid clustering. It is mixed with the prepared agarose gel and formed with a 2 mm glass capillary in a cylinder shape for easy holding. Once solidified, the gel is pushed out with a plunger into ethanol for dehydration. The dehydration process is done in three steps using 20%, 50% and 100%

ethanol for 15 min, 15 min and 30 min, respectively. After dehydration, the agarose gel is transferred to the final RI-matching solvent for at least 1 day. Once RI-matched, the agarose is transferred to the same capillary or glued to a sample holder for PSF measurement. For the PSF measurement, we imaged the nanoparticles using a 561-nm laser line with a power of 0.5 mW, a z-step size of 380 nm, and a 20-pixel camera rolling shutter. All parameters corresponded to the same slit size and z-step as used for imaging the biological samples. The PSF is then determined based on the full-width at half-maximum of the intensity profiles of the recorded nanoparticles using Fiji³⁹.

Closed-loop monitoring arm with a PSD

We have used a PSD (Thorlabs, cat no. PDP90A) with a K-Cube controller (Thorlabs, cat. no. KPA101) in combination with a compact probe laser module with a Gaussian intensity profile (1 mW laser, 635 nm; Thorlabs, cat. no. PL202). The PSD and probe laser are positioned at 45 degrees relative to the optical axis of the ASLM unit. The laser is reflected on the ASLM mirror and hits the PSD. The axial movement (along the optical axis) of the voice coil translates into the lateral movement of the laser spot on the PSD. By tracking the center position of the laser beam on the PSD, the output voltage of the K-Cube controller (Output X) generates a corresponding signal with an accuracy of 0.7 μ m at a wavelength of 635 nm (approximately 100 μ W at the PSD). To achieve this level of accuracy, we have used an absorptive neutral density filter with 10% transmission (Thorlabs, cat. no. NE510A, half-inch diameter) attached to the PSD. It should be noted that the closed-loop monitoring is used only during calibration to optimize the voice coil waveform for the desired scan frequency. During actual imaging, the system operates with the precalibrated waveform.

The output of the K-Cube is connected to a compact multi-function generator (Moku:Go, Liquid Instruments), which streams the PSD output directly to the controlling computer for further analysis (Supplementary Fig. 8). The signal is then processed using a Python script that calculates the residual of the PSD output compared to the initial linear waveform and generates a corrective waveform. The corrective signal is sent to the voice coil via a function generator. The system operates using a feedback closed-loop algorithm, which works by either converging to a predefined metric or incorporating user feedback based on the swept beam quality (Supplementary Note 4). The best corrective waveform is selected, typically achieved in fewer than ten iterations. Ultimately, the optimal corrective waveform for each target frequency needs to be calculated only once.

Field curvature measurement

To measure the light-sheet field curvature, we used the PSF measurement and direct imaging of the light-sheet cross-section. The PSF measurement was the same as described. However, for the light-sheet cross-section measurement, we used a small mirror of 2 mm \times 2 mm glued to a glass capillary. The mirror is placed in the chamber between the objective lenses at 45 degrees, directly reflecting the light sheet into the detection arm. Without any field curvature, the cross-section of the light sheet should be a straight line from top to bottom of the FOV. However, in the presence of field curvature, the light-sheet thickness varies along the FOV height. To measure the field curvature, we first parked the light sheet in the center of the detection FOV (the voice coil was parked at the center position with zero amplitude). Then, the light-sheet cross-section is recorded in several positions by gently moving the mirror along the FOV. The intensity profile of the light sheet for recorded cross-sections is measured from top to bottom. Then, the thinnest light sheet in each plane along the FOV height is selected. The relation between these thinnest parts of the light sheet describes the field curvature.

Animals

Animal handling complied with relevant national and international guidelines for the care and use of laboratory animals in research

(European Guideline for Animal Experiments 2010/63/EU) and in accordance with regulations put forward by the state authorities of Lower Saxony (LAVES) and Schleswig-Holstein (MLLEV). The mice were kept at a constant temperature (22 °C) and humidity (50%) on a 12-h light/dark cycle and were provided with standard laboratory chow and water ad libitum as well as enrichment. Mice euthanized for extracting cochleae and brains in this study aided the development of the new microscope presented here, capable of high-throughput and high-resolution submicron imaging to further address various biological questions in following studies. Mice for brain extraction were bred at the local animal facility of the University of Lübeck. Male C57BL/6/N mice at the age of 4–6 months were used. Adult zebrafish (*Danio rerio*), embryos and larvae were maintained following established protocols. Adult fish were kept at a water temperature of 26.0 °C and a 14 h/10 h light/dark cycle. Fish were fed standard laboratory food supplemented with live *Artemia* larvae. The transgenic line *Tg(kdrl:GFP)* was used, where green fluorescent protein (GFP) is expressed in the vascular endothelium. Zebrafish embryos were kept at 28.0 °C in 0.3× Daniae's medium with 0.003% 1-phenyl-2-thiourea added at 1 dpf to suppress pigmentation. Embryos were checked for potential malformations and expression of the endogenous reporter using a fluorescence stereomicroscope. Larval zebrafish at 3 dpf showing the desired expression pattern and without apparent malformations were selected for sample preparation.

Sample preparation (mouse cochlea)

After extraction from the temporal bone, cochleae were fixed for 45 min in 4% formaldehyde, subsequently rinsed in phosphate-buffered saline (PBS) and decalcified for up to 1 week in 10% ethylenediaminetetraacetic acid (pH 8). During decalcification, cochleae were trimmed continuously with surgical instruments (Fine Science Tools) using a bright field microscope (Zeiss; Olympus SZ61) to remove as much bone as possible for easy access and later penetration of the light-sheet beam during optical sectioning.

Immunolabeling and tissue clearing (mouse cochlea)

For robust and reproducible immunolabeling as well as optical clearing, we used a newly adapted version of the optimized iDISCO⁺ clearing protocol adapted to the cochlea¹⁰ (cDisco⁺). Here we first decalcified the mouse cochlea for 4 days using 10% ethylenediaminetetraacetic acid of pH 8.0 at room temperature. Second, we decolorized the decalcified specimen for up to 3 days at 37 °C using 25% amino alcohol (N,N,N,N'-Tetrakis(2-Hydroxypropyl)ethylenediamine). Next we employed pretreatment and permeabilization of the samples for approximately 4 days according to iDisco¹⁹, specifically without the use of methanol, followed by epitope blocking at 37 °C. For reliable immunolabeling of the entire population of SGNs within the Rosenthal canal, sufficient penetration of the cochlea was achieved by incubating each antibody for 14 days at 37 °C followed by washing in PBS-Tween 0.2% with Heparin 10 μ g ml⁻¹ for up to 1 day¹⁰. Here we used a guinea pig polyclonal anti-PV antibody (Synaptic Systems, cat. no. 195 004; lot no. 3-38; clone not specified) at a dilution of 1:300, preconjugated with a camelid single domain anti-guinea pig antibody labeled with Atto565 (NanoTag Biotechnologies, cat. no. N0602; lot no. 022205; clone not specified) at a molar ratio of 1:3. Further, we used a monoclonal mouse anti-neurofilament 200 (NF200) antibody (Sigma-Aldrich, cat. no. N5389; lot no. 099M4843V; clone NE14) at a dilution of 1:400 and a polyclonal rabbit anti-vesicular glutamate transporter 3 (VGAT3) antibody (Synaptic Systems, cat. no. 135 203; lot no. 1-47; clone not specified) at a dilution of 1:300. For a secondary staining staining an anti-mouse antibody labeled with Alexa 647 (Invitrogen, cat. no. A-21236; lot no. 751096; clone not specified) and an anti-rabbit antibody labeled with Alexa 488 (Invitrogen, cat. no. A-11008; lot no. 659082; clone not specified), each at a dilution of 1:200 were used. Following the immunolabeling, the cochleae were dehydrated, stepwise, in a methanol/H₂O series ranging

from 20% to 100% methanol for up to 1 day and then delipidized with dichloromethane at room temperature⁴¹. Finally, RI-matching was performed by initial embedding in dibenzyl ether for 1 day and consecutive transfer to ECi for storage and imaging at room temperature.

Sample mounting (mouse cochlea)

For imaging and sufficient matching of the RI the cleared cochleae remained in ECi for at least 6 days. The cochleae were then mounted carefully on a customized 3D-printed sample holder. Here we clamped the cochlea dorsal of its basal turn at the attached vestibular system to the holder and inserted the mounted cochleae with the cochlear apex facing the bottom of the imaging chamber. Thus, the modiolus of the cochlea is placed approximately perpendicular to the applied light-sheet beam within the imaging chamber.

Mouse brain

The whole procedure of preparing, staining and clearing the tissue was performed according to a published protocol⁴² with slight adaptations. The method is based on the iDISCO procedure and optimized to visualize the brain vasculature. Briefly, after decapitation, the samples were extracted by opening the skull and removing the brain, ideally including the meninges and surface vessels. In addition to perfusion fixation using 4% paraformaldehyde in PBS, a postfixation period of 3 h at room temperature followed the brain extraction. The tissue was dehydrated using ascending methanol concentrations and incubated in 100% methanol for 2 h at room temperature. Lipids were extracted by incubation in dichloromethane:methanol (2:1) overnight at room temperature and samples were bleached using 5% H₂O₂ in methanol overnight at 4 °C. Rehydration was performed by descending methanol concentrations and samples were kept for 24 h at 37 °C in PBS/0.01% sodium azide. Blocking was performed using PBS supplemented with Triton-X 0.2% and porcine gelatin 0.2% for 24 h at 37 °C. Subsequent incubation with primary antibodies lasted for 10 days at 37 °C in the blocking solution. Here primary antibodies included antibodies detecting smooth muscle cells by using anti- α SMA directly coupled to Cy3 (Millipore, cat. no. C6198, 3.75 μ g ml⁻¹) and antibodies detecting endothelial cells by using anti-podocalyxin (R&D systems, cat. no. MAB1556, 0.5 μ g ml⁻¹) and anti-CD31 (R&D systems, cat. no. AF3628, 0.133 μ g ml⁻¹). After washing overnight, secondary antibodies were then incubated for another 7 days at 37 °C. For comprehensive staining of all endothelial cells in the brain, both primary antibodies were combined and visualized by secondary antibodies carrying the same fluorophore. We used anti-goat and anti-rat secondary antibodies coupled to Alexa 647 (Invitrogen, cat. no. A21447, 2.5 μ g ml⁻¹ and Abcam, ab150155, 2.5 μ g ml⁻¹, respectively). SMA staining did not include a secondary antibody since the primary antibody is directly coupled to Cy3. After staining, the brains were cleared starting with another dehydration and washing in a dichloromethane/methanol mixture as described above. Benzyl ether was used to optically clear and then transfer to ECi for storage and imaging at room temperature.

Tissue clearing and sample mounting (zebrafish)

Hatched *Tg(kdrl:GFP)* zebrafish at 3 dpf were anesthetized using 0.02% MS222 and fixed in 4% paraformaldehyde in PBS overnight followed by several washes in PBS. For clearing of the zebrafish larvae, we used an adjusted version of the EZ Clear protocol²⁰. The specimens were delipidated in EZ Clear solution (50% tetrahydrofuran in Milli-Q water) for 2 h at room temperature, followed by washes in Milli-Q. RI matching was performed with an adjusted EZ View solution. As reported in the original protocol, the RI of the EZ View solution can be tuned by using different concentrations of urea. Starting at 1.2 M urea, the RI of the EZ View solution was monitored using a digital refractometer (Krüss cat. no. DR301-95; A. Krüss Optronic GmbH) while small amounts of urea were added and dissolved until an RI of $n_D = 1.473$ (refractive index of glass capillary) was reached (if the RI is too high, it can be decreased by

adding 0.2× PBS). This RI was chosen because it allowed for the convenient mounting of delicate samples and immersion as follows: samples were transferred to a gel consisting of 1.5% low-gelling point agarose in the RI-tuned EZ View and drawn into borosilicate glass capillaries ($n_D = 1.473$; ID = 1.0 mm, OD = 1.5 mm, BRAND, cat. no. 701904). The RI of the gel was confirmed before mounting and adjusted by adding Milli-Q if necessary. After gelation of the EZ View agarose, the capillaries were sealed at the bottom with plasticine. Because of the identical RI, glycerol was used as immersion medium as it is inexpensive and does not dry out to form a sticky film and is easier to clean than EZ View.

Reporting summary

Further information on research design is available in the Nature Portfolio Reporting Summary linked to this article.

Data availability

Due to the very large size of the imaging datasets generated in this study, a downsampled version of the complete stitched dataset, together with a representative high-resolution subset, is available via Zenodo at <https://doi.org/10.5281/zenodo.17080861> (ref. 43). The full original high-resolution dataset is available from the corresponding author upon reasonable request. The CAD models of the custom parts are available via Zenodo at <https://doi.org/10.5281/zenodo.17396943> (ref. 44).

Code availability

The Python script for the voice coil waveform corrector is available via GitHub at <https://github.com/aakhtemostafa/Voice-Coil-Waveform-Correction.git> (ref. 45).

References

39. Schindelin, J. et al. Fiji: an open-source platform for biological-image analysis. *Nat. Methods* **9**, 676–682 (2012).
40. Hörl, D. et al. BigStitcher: reconstructing high-resolution image datasets of cleared and expanded samples. *Nat. Methods* **16**, 870–874 (2019).
41. Renier, N. et al. Mapping of brain activity by automated volume analysis of immediate early genes. *Cell* **165**, 1789–1802 (2016).
42. Kirst, C. et al. Mapping the fine-scale organization and plasticity of the brain vasculature. *Cell* **180**, 780–795 (2020).
43. Aakhte, M. et al. Isotropic, aberration-corrected light sheet microscopy for rapid high-resolution imaging of cleared tissue. Zenodo <https://doi.org/10.5281/zenodo.17080860> (2025).
44. Aakhte, M. CAD files of the isotropic, aberration-corrected light sheet microscope. Zenodo <https://doi.org/10.5281/zenodo.17396943> (2025).
45. Aakhte, M. Voice-coil-waveform-correction. GitHub <https://github.com/aakhtemostafa/Voice-Coil-Waveform-Correction.git> (2025).

Acknowledgements

We thank C. Schmidt and his team at the central mechanical workshop of the Department of Physics at the University of Göttingen for their invaluable assistance in creating mechanical components. We also acknowledge K. Adner for several electronic components, P. Maier for his constructive input on the microscope development and T. Quilitz for her feedback on imaging mouse cochlea. We thank R. Fiolka and K. Dean for their insightful discussions on selecting the voice coil. We thank P. Lenart, M. A. Eskandari and R. Tsukanov for providing the Hamamatsu camera and frame grabber. We thank B. Lembrich and Z. S. Gilani, both from Lübeck, as well as I. Preuss and S. Langer of the Göttingen InnerEarLab for their expert technical support and B. Wolf and J. Neef for scientific discussion. We further acknowledge funding by the Alexander von Humboldt Foundation (J.H.; AvH professorship, including T.G.'s position) and the German Center for Cardiovascular Research (DZHK; 81X2300302) on behalf of M.A..

J.W. and J.H. M.A., G.F.M., J.H. and T.M. are supported by the MWK (Niedersächsisches Ministerium für Wissenschaft und Kultur). We further acknowledge the support by the German Research Foundation via the Cluster of Excellence Multiscale Bioimaging (MBExC; EXC 2067/1-390729940) and its Hertha Sponer College at the University of Göttingen (M.A., G.F.M., L.R., A.M.D., T.M. and J.H.) as well as the collaborative research center 889 (L.R.). The work was additionally funded by the Else Kröner Fresenius Foundation through the Else Kröner Fresenius Center for Optogenetic Therapies (to J.H. and T.M.), European Union (ERC, 'DynaHear,' grant agreement no. 101054467), and the Fondation Pour l'Audition (FPA RD-2020-10) to T.M. The mouse brain experiments were supported by a grant from the Deutsche Forschungsgemeinschaft to J.W. (WE 6456/1-1).

Author contributions

M.A. and J.H. designed the research. M.A. designed and built the optical setup and developed preview tiling Python script. G.F.M. and J.L. developed the TCP/IP pipeline for controlling microscope remotely. J.L. wrote the microscope control system software. M.A., K.R.W. and J.H. evaluated possible light-sheet microscope configuration. T.G. prepared zebrafish. L.R. and A.M.D. prepared mouse cochlea. J.W. prepared mouse brains. M.A. and T.G. optimized sample mounting. M.A. performed imaging and postprocessing, with input from T.G., J.W. and J.H. M.A. performed image analysis with input from T.G., J.W., T.M. and J.H. T.G., L.R., A.M.D., J.W., T.M. and J.H. provided feedback on microscope performance. T.M. provided resources for

the mouse cochlea experiment. J.W. and M.S. provided resources for the mouse brain experiment. J.H. provided resources for the zebrafish experiment. M.A. and J.H. wrote the paper, with input from all authors. J.H. directed and provided resources for the entire research.

Funding

Open access funding provided by Georg-August-Universität Göttingen.

Competing interests

T.M. is cofounder of the OptoGenTech Company. The other authors declare no competing interests.

Additional information

Supplementary information The online version contains supplementary material available at <https://doi.org/10.1038/s41587-025-02882-8>.

Correspondence and requests for materials should be addressed to Mostafa Aakhte or Jan Huisken.

Peer review information *Nature Biotechnology* thanks Raju Tomer and the other, anonymous, reviewer(s) for their contribution to the peer review of this work.

Reprints and permissions information is available at www.nature.com/reprints.

Reporting Summary

Nature Portfolio wishes to improve the reproducibility of the work that we publish. This form provides structure for consistency and transparency in reporting. For further information on Nature Portfolio policies, see our [Editorial Policies](#) and the [Editorial Policy Checklist](#).

Statistics

For all statistical analyses, confirm that the following items are present in the figure legend, table legend, main text, or Methods section.

n/a Confirmed

- The exact sample size (n) for each experimental group/condition, given as a discrete number and unit of measurement
- A statement on whether measurements were taken from distinct samples or whether the same sample was measured repeatedly
- The statistical test(s) used AND whether they are one- or two-sided
Only common tests should be described solely by name; describe more complex techniques in the Methods section.
- A description of all covariates tested
- A description of any assumptions or corrections, such as tests of normality and adjustment for multiple comparisons
- A full description of the statistical parameters including central tendency (e.g. means) or other basic estimates (e.g. regression coefficient) AND variation (e.g. standard deviation) or associated estimates of uncertainty (e.g. confidence intervals)
- For null hypothesis testing, the test statistic (e.g. F , t , r) with confidence intervals, effect sizes, degrees of freedom and P value noted
Give P values as exact values whenever suitable.
- For Bayesian analysis, information on the choice of priors and Markov chain Monte Carlo settings
- For hierarchical and complex designs, identification of the appropriate level for tests and full reporting of outcomes
- Estimates of effect sizes (e.g. Cohen's d , Pearson's r), indicating how they were calculated

Our web collection on [statistics for biologists](#) contains articles on many of the points above.

Software and code

Policy information about [availability of computer code](#)

Data collection	The custom codes developed in this study have been deposited in the public repository GitHub (https://github.com/aakhtemostafa/Voice-Coil-Waveform-Correction.git).
Data analysis	Data and image processing, and visualization were performed using open-source and commercial software. Initial image analysis was conducted using Fiji, while stitching and conversion to HDF5 were carried out with BigStitcher. 3D data visualization was performed using Imaris 9.7. Point spread function measurements were obtained using a custom Python script and Fiji, and the resolution calculations for the detection objective lens were performed in MATLAB. The scripts are available from the authors upon request.

For manuscripts utilizing custom algorithms or software that are central to the research but not yet described in published literature, software must be made available to editors and reviewers. We strongly encourage code deposition in a community repository (e.g. GitHub). See the Nature Portfolio [guidelines for submitting code & software](#) for further information.

Data

Policy information about [availability of data](#)

All manuscripts must include a [data availability statement](#). This statement should provide the following information, where applicable:

- Accession codes, unique identifiers, or web links for publicly available datasets
- A description of any restrictions on data availability
- For clinical datasets or third party data, please ensure that the statement adheres to our [policy](#)

Due to the very large size of the imaging datasets generated in this study, a down-sampled version of the complete stitched dataset together with a representative high-resolution subset has been deposited in Zenodo (<https://doi.org/10.5281/zenodo.17080861>). The full original high-resolution dataset is available from the corresponding author upon reasonable request.

The CAD models of the custom parts are available at the following link: <https://doi.org/10.5281/zenodo.17396943>

Research involving human participants, their data, or biological material

Policy information about studies with [human participants or human data](#). See also policy information about [sex, gender \(identity/presentation\), and sexual orientation](#) and [race, ethnicity and racism](#).

Reporting on sex and gender

Use the terms sex (biological attribute) and gender (shaped by social and cultural circumstances) carefully in order to avoid confusing both terms. Indicate if findings apply to only one sex or gender; describe whether sex and gender were considered in study design; whether sex and/or gender was determined based on self-reporting or assigned and methods used. Provide in the source data disaggregated sex and gender data, where this information has been collected, and if consent has been obtained for sharing of individual-level data; provide overall numbers in this Reporting Summary. Please state if this information has not been collected. Report sex- and gender-based analyses where performed, justify reasons for lack of sex- and gender-based analysis.

Reporting on race, ethnicity, or other socially relevant groupings

Please specify the socially constructed or socially relevant categorization variable(s) used in your manuscript and explain why they were used. Please note that such variables should not be used as proxies for other socially constructed/relevant variables (for example, race or ethnicity should not be used as a proxy for socioeconomic status). Provide clear definitions of the relevant terms used, how they were provided (by the participants/respondents, the researchers, or third parties), and the method(s) used to classify people into the different categories (e.g. self-report, census or administrative data, social media data, etc.) Please provide details about how you controlled for confounding variables in your analyses.

Population characteristics

Describe the covariate-relevant population characteristics of the human research participants (e.g. age, genotypic information, past and current diagnosis and treatment categories). If you filled out the behavioural & social sciences study design questions and have nothing to add here, write "See above."

Recruitment

Describe how participants were recruited. Outline any potential self-selection bias or other biases that may be present and how these are likely to impact results.

Ethics oversight

Identify the organization(s) that approved the study protocol.

Note that full information on the approval of the study protocol must also be provided in the manuscript.

Field-specific reporting

Please select the one below that is the best fit for your research. If you are not sure, read the appropriate sections before making your selection.

Life sciences Behavioural & social sciences Ecological, evolutionary & environmental sciences

For a reference copy of the document with all sections, see nature.com/documents/nr-reporting-summary-flat.pdf

Life sciences study design

All studies must disclose on these points even when the disclosure is negative.

Sample size

We did not calculate sample sizes beforehand. To ensure reliable estimation of PSF parameters across the field of view (FOV), we measured the full width at half maximum (FWHM) of seven nano-gold beads per FOV section, resulting in more than 300 beads in total in ASLM mode with and without the concave mirror. The beads were embedded in cleared, refractive-index-matched agarose within the chamber medium. For the mouse brain, cochlea, and zebrafish experiments, we did not use a statistical method to determine the number of samples. Instead, we imaged as many samples as were sufficient to demonstrate reproducibility and validate our imaging approach.

Data exclusions

No data was excluded.

Replication

Replication of the experiment on all imaged samples was successful.

Randomization	The PSF measurements were taken randomly across the large field of view.
Blinding	Not applicable. The manuscript describes a new imaging method.

Reporting for specific materials, systems and methods

We require information from authors about some types of materials, experimental systems and methods used in many studies. Here, indicate whether each material, system or method listed is relevant to your study. If you are not sure if a list item applies to your research, read the appropriate section before selecting a response.

Materials & experimental systems		Methods	
n/a	Involved in the study	n/a	Involved in the study
<input type="checkbox"/>	<input checked="" type="checkbox"/> Antibodies	<input checked="" type="checkbox"/>	<input type="checkbox"/> ChIP-seq
<input checked="" type="checkbox"/>	<input type="checkbox"/> Eukaryotic cell lines	<input checked="" type="checkbox"/>	<input type="checkbox"/> Flow cytometry
<input checked="" type="checkbox"/>	<input type="checkbox"/> Palaeontology and archaeology	<input checked="" type="checkbox"/>	<input type="checkbox"/> MRI-based neuroimaging
<input type="checkbox"/>	<input checked="" type="checkbox"/> Animals and other organisms		
<input checked="" type="checkbox"/>	<input type="checkbox"/> Clinical data		
<input checked="" type="checkbox"/>	<input type="checkbox"/> Dual use research of concern		
<input checked="" type="checkbox"/>	<input type="checkbox"/> Plants		

Antibodies

Antibodies used

Mouse Cochlea:

Guinea pig polyclonal anti-parvalbumin antibody (Synaptic Systems, Cat.: 195 004; Lot # 3-38; Clone not specified) – dilution: 1:300 Camelid single domain anti-guinea pig antibody (NanoTag Biotechnologies, Cat.: N0602; Lot # 022205; Clone not specified) labelled with Atto565 – pre-conjugated with 195 004 (Synaptic Systems, see before) at a molar ratio of 1:3.

Multicolor imaging of mouse cochlea: guinea pig anti-parvalbumin (Synaptic Systems, Cat.: 195 004) and the camelid single domain anti-guinea pig antibody (NanoTag Biotechnologies, Cat.: N0602) were used as described before. Additionally, a monoclonal mouse anti-neurofilament 200 antibody (Sigma-Aldrich, Cat.: N5389; Lot # 099M4843V; Clone NE14) at a dilution of 1:400 and a polyclonal rabbit anti-vesicular glutamate transporter 3 antibody (Synaptic Systems, Cat.: 135 203; Lot # 1-47; Clone not specified) at a dilution of 1:300 were used.. For the corresponding secondary staining staining an anti-mouse antibody labelled with Alexa 647 (Invitrogen, Cat.: A-21236; Lot # 751096; Clone not specified) and an anti-rabbit antibody labelled with Alexa 488 (Invitrogen; Cat.: A-11008; # 659082; Clone not specified), were used, each at a dilution of 1:200..

Mouse brain:

Anti- α smooth muscle actin (α SMA) – Directly coupled to Cy3 (Millipore, C6198, 3.75 μ g/ml, clone 1A4) - Used for detecting smooth muscle cells (validation: original publication: Skalli, O., et al. A monoclonal antibody against alpha-smooth muscle actin: a new probe for smooth muscle differentiation. *J Cell Biol* 103, 2787-2796 (1986).)

Anti-podocalyxin (R&D Systems, MAB1556, 0.5 μ g/ml, clone 192703) - Used for detecting endothelial cells (validation: Monoclonal antibody used by numerous studies according to manufacturer, validated by the staining pattern)

Anti-CD31 (R&D Systems, AF3628, 0.133 μ g/ml, lot not recorded) - Used for detecting endothelial cells (validation: Polyclonal antibody used by numerous studies according to manufacturer, validated by the staining pattern)

Anti-goat secondary antibody coupled to Alexa647 (Invitrogen, A21447, 2.5 μ g/ml, lot: 2297623)

Anti-rat secondary antibody coupled to Alexa647 (Abcam, ab150155, 2.5 μ g/ml, lot: 2465077)

Validation

The usage of all primary antibodies is described in the Methods section for both mouse cochlea and mouse brain preparations.

- Mouse cochlea:

Used for immunofluorescence staining in mouse cochlear tissue.

Duque Afonso CJ: Development and Application of Tools for the Characterization of the Optogenetics Stimulation of the Cochlea. PhD Thesis. 2020; <http://dx.doi.org/10.53846/goediss-8106>

- Mouse brain:

• anti- α SMA: Used for immunofluorescence staining of smooth muscle actin in mouse brain vasculature; validated by Skalli, O., et al. A monoclonal antibody against alpha-smooth muscle actin: a new probe for smooth muscle differentiation. *J Cell Biol* 103, 2787–2796 (1986).

• anti-CD31: Used for immunofluorescence staining of endothelial cells in mouse brain tissue; validated by Western blotting according to manufacturer and by staining pattern; widely used in published studies.

• anti-podocalyxin: Used for immunofluorescence staining of vascular structures in mouse brain tissue; validated by immunocytochemistry according to manufacturer and by staining pattern; widely used in published studies.

Animals and other research organisms

Policy information about [studies involving animals](#); [ARRIVE guidelines](#) recommended for reporting animal research, and [Sex and Gender in Research](#)

Laboratory animals

Mouse cochlea: *Mus musculus*, C57BL/6J. The mice were kept at a constant temperature of 22–24°C and at a relative humidity level of 45 to 65% on a 12-hour light/ dark cycle and were provided with enrichment, and access to food and water *ad libitum*. Mice for extraction of cochleae were bred at the local animal facility of the University Medical Center Göttingen. Here, we used C57BL/6J wild-type mice of both sexes of 1–2 months.

Mouse Brain: C57BL/6N mice (bred in the animal facility of the University of Lübeck). The mice were kept at a constant temperature (22°C) and humidity (50%) on a 12-hour light/ dark cycle and were provided with standard laboratory chow and water *ad libitum*. Mice for brain extraction were bred at the local animal facility of the University of Lübeck. Male C57BL6/N mice at the age of 4–6 months were used.

Zebrafish: transgenic line Tg(kdrl:GFP), 3 dpf

Wild animals

/

Reporting on sex

Mouse Cochlea: Animals of both sexes were used.
 Mouse Brain: both sexes were used for establishing stainings and clearing, no difference was observed, images in the manuscript originate from male mice
 Zebrafish: The sex cannot be determined at this early stage of development.

Field-collected samples

/

Ethics oversight

In Germany organ extraction is operated under §4 of the animal welfare act and not requiring specific permission of the responsible authorities. Following internal regulations, approval for extraction of cochleae was obtained from the animal welfare office of the University Medical Center (UMG) Göttingen. At University Medical Center Göttingen animals for this study were strictly sacrificed for organ collection only. Thus, a license by the authorities was not required. It was performed according to the regulations of the internal animal welfare office. Experimental procedures were approved by the local animal ethics committee (Ministerium für Landwirtschaft, Umwelt und ländliche Räume, Kiel, Germany).

Adult zebrafish (*Danio rerio*), embryos and larvae were maintained following established protocols in compliance with EU directive 2010/63/EU and the German Animal Welfare Act and approved by the authorities of Lower Saxony (Niedersächsisches Landesamt für Verbraucherschutz und Lebensmittelsicherheit, Oldenburg, Germany).

Note that full information on the approval of the study protocol must also be provided in the manuscript.

Plants

Seed stocks

Report on the source of all seed stocks or other plant material used. If applicable, state the seed stock centre and catalogue number. If plant specimens were collected from the field, describe the collection location, date and sampling procedures.

Novel plant genotypes

Describe the methods by which all novel plant genotypes were produced. This includes those generated by transgenic approaches, gene editing, chemical/radiation-based mutagenesis and hybridization. For transgenic lines, describe the transformation method, the number of independent lines analyzed and the generation upon which experiments were performed. For gene-edited lines, describe the editor used, the endogenous sequence targeted for editing, the targeting guide RNA sequence (if applicable) and how the editor was applied.

Authentication

Describe any authentication procedures for each seed stock used or novel genotype generated. Describe any experiments used to assess the effect of a mutation and, where applicable, how potential secondary effects (e.g. second site T-DNA insertions, mosaicism, off-target gene editing) were examined.